

Understanding the Key Roles of pH Buffer in Accelerating Lignin Degradation by Lignin Peroxidase

Wenhan Fang, Shishi Feng, Zhihui Jiang, Wanzhen Liang, Pengfei Li,* and Binju Wang*



Cite This: *JACS Au* 2023, 3, 536–549



Read Online

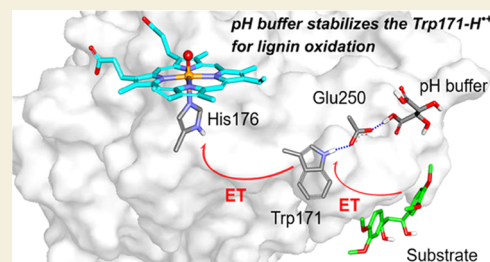
ACCESS |

Metrics & More

Article Recommendations

Supporting Information

ABSTRACT: pH buffer plays versatile roles in both biology and chemistry. In this study, we unravel the critical role of pH buffer in accelerating degradation of the lignin substrate in lignin peroxidase (LiP) using QM/MM MD simulations and the nonadiabatic electron transfer (ET) and proton-coupled electron transfer (PCET) theories. As a key enzyme involved in lignin degradation, LiP accomplishes the oxidation of lignin via two consecutive ET reactions and the subsequent C–C cleavage of the lignin cation radical. The first one involves ET from Trp171 to the active species of Compound I, while the second one involves ET from the lignin substrate to the Trp171 radical. Differing from the common view that pH = 3 may enhance the oxidizing power of Cpd I via protonation of the protein environment, our study shows that the intrinsic electric fields have minor effects on the first ET step. Instead, our study shows that the pH buffer of tartaric acid plays key roles during the second ET step. Our study shows that the pH buffer of tartaric acid can form a strong H-bond with Glu250, which can prevent the proton transfer from the Trp171-H^{•+} cation radical to Glu250, thereby stabilizing the Trp171-H^{•+} cation radical for the lignin oxidation. In addition, the pH buffer of tartaric acid can enhance the oxidizing power of the Trp171-H^{•+} cation radical via both the protonation of the proximal Asp264 and the second-sphere H-bond with Glu250. Such synergistic effects of pH buffer facilitate the thermodynamics of the second ET step and reduce the overall barrier of lignin degradation by ~4.3 kcal/mol, which corresponds to a rate acceleration of 10³-fold that agrees with experiments. These findings not only expand our understanding on pH-dependent redox reactions in both biology and chemistry but also provide valuable insights into tryptophan-mediated biological ET reactions.



KEYWORDS: long-range electron transfer, pH effects, lignin peroxidase, QM/MM MD simulations, nonadiabatic ET and PCET

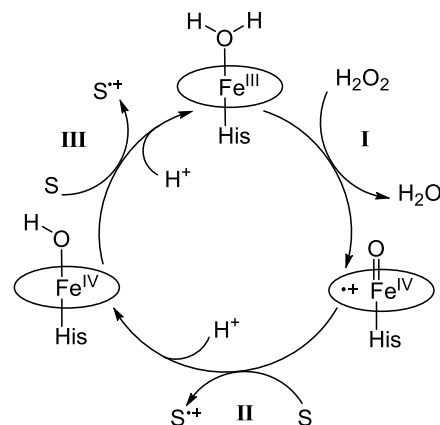
1. INTRODUCTION

pH buffers play vital roles in biology and chemistry. For instance, pH buffers can change the protonation/deprotonation of the electron donor/acceptor directly,^{1,2} through which one could modulate the redox potential of the electron donor/acceptor. However, the exact roles of pH buffer are still elusive for many enzymatic reactions. Herein, we address these issues in lignin peroxidase,^{3,4} a key enzyme involved in lignin degradation.

In nature, several peroxidases are found to be responsible for the degradation of lignin, including the versatile peroxidase (VP),^{5,6} manganese peroxidase (MnP),⁷ and lignin peroxidase (LiP).^{4,8–11} As a peroxidase, LiP catalyzes the cleavage of ether C–C and C–O bonds in lignin via a H₂O₂-dependent oxidative mechanism. Compared to many other peroxidases, LiP can oxidize the less-reactive nonphenolic lignin subunits.^{4,9,10}

As shown in Scheme 1, the catalytic cycle of LiP involves three main stages.^{4,11} Similar to other peroxidases, the first stage (I) involves the activation by H₂O₂ to form a ferryl ion porphyrin π -cation radical species, so-called Compound I (Cpd I), a common active species in peroxidases.^{10,12–14} In the second stage (II), Cpd I performs one-electron oxidation of

Scheme 1. An Abbreviated Catalytic Cycle of Lignin Peroxidase

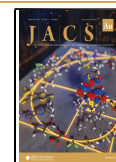


Received: November 30, 2022

Revised: January 4, 2023

Accepted: January 5, 2023

Published: January 24, 2023



the lignin substrate, yielding Cpd II and the lignin cation radical species ($S^{\bullet+}$). Emerging from this lignin cation radical species, C–C cleavage can occur to generate the lignin fragments. In the third stage (III), Cpd II can perform a second-round oxidation of the lignin substrate, returning the enzyme to the native ferric state. Currently, it is widely accepted that the oxidation of lignin by Cpd I/II involves a long-range electron transfer (ET) from the lignin substrate to Cpd I/II.^{4,9,10,14–19} Such long-range ET is mediated by a redox-active tryptophan residue exposed at the protein surface. In both VP and LiP, a tryptophan radical (Trp171 in LiP and Trp164 in VP) has been characterized by EPR spectroscopy,^{20–24} suggesting that the oxidation of lignin may occur via two long-range ET steps mediated by Trp171 (see Figure 1).

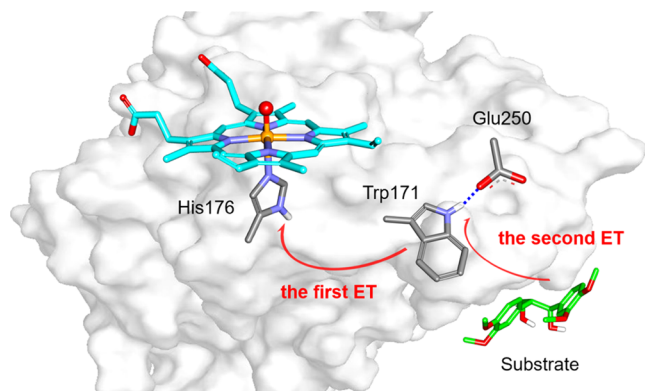


Figure 1. Two consecutive long-range ET steps mediated by Trp171. These two ET steps are involved in the first-round oxidation of the lignin substrate by LiP (stage II in Scheme 1).

One involves ET from Trp171 to Cpd I, while the other involves ET from the lignin substrate to the Trp171 radical. However, the mechanism of long-range ET reactions, either through outer-sphere ET or through proton-coupled electron transfer (PCET), is elusive.^{1,2,25–32}

In addition to the unsolved ET mechanism in LiP, a long-standing issue exists for the pH-dependent reactivity of LiP. Specifically, it was found that the degradation of the lignin substrate can be enhanced by $\sim 10^3$ -fold when changing pH = 7 to the optimal pH = 3.³³ To rationalize this puzzle, various explanations have been proposed. For instance, it was proposed that low pH can protonate the titratable residues close to Heme, which may increase the redox potential of Cpd I, thereby increasing the oxidizing power of Cpd I toward lignin oxidation.³⁴ However, an increase of the Cpd I redox potential can only increase the driving force for the first ET step (Trp171 \rightarrow Cpd I), while the thermodynamics of the second ET step (lignin \rightarrow Trp171) may not be affected. Thus, it is enigmatic how pH buffer is involved in LiP catalysis.

To elucidate the mechanism of LiP catalysis and pH effects on the ET rate, we performed QM/MM MD simulations and the nonadiabatic ET and PCET calculations on the one-electron oxidation of lignin mediated by Cpd I (stage II in Scheme 1). Our study provided a molecular basis on how pH buffer accelerates the lignin degradation by LiP, highlighting that the engineering of the second-sphere H-bonding interactions and the proximal protonation states can be used as practical strategies to regulate the kinetics of the ET reactions.

2. METHODS

2.1. System Setup and Classical MD Simulations

The structure of LiP was constructed based on the crystal structure of the native LiP from *P. chrysosporium* (PDB entry: 1B80, which was obtained at pH = 3.5 and with a resolution of 1.73 Å).³⁵ The *P. chrysosporium* LiP has been extensively studied by experiments, which has well-characterized crystal structures and biochemical data,^{6–12,36,37} providing an excellent example for comparison with theoretical studies. Only chain A was retained in our study. The β -hydroxy-Trp171 was converted back to a normal Trp residue. The dimeric lignin substrate (i.e., 1,2-bis(3,4-dimethoxyphenyl)-1,3-propanediol) was docked into the proximity of Trp171, while tartaric acid was docked into the proximity of Glu250. Notably, as our simulations focus on the interaction of Glu250 with a protonated carboxylic group of tartaric acid, either the singly protonated or the doubly protonated form would be reasonable for our simulations. In the present study, we treated the tartaric acid doubly protonated in our simulations. All dockings were performed using the AutoDock Vina tool³⁶ in Chimera.³⁸ We assigned the protonation states of titratable residues (His, Glu, Asp) based on the calculated pK_a values by PROPKA software³⁹ and pH = 3 or 7. The protonation states were further checked by visual inspection of the local hydrogen-bond networks. Especially, Glu250 was deprotonated, while protonation states of the other titratable residues are provided in the Supporting Information (SI). The pK_a values can also be reliably predicted by the constant pH MD simulations.^{40,41} Nevertheless, the parameterization of non-standard residues (such as heme-Cpd I) for our current system can be a difficult task. For heme propionic groups, we assigned them as the deprotonated states since the pK_a values of surrounding titratable residues are higher than 3 according to the PROPKA calculation. To further confirm such an assignment, we have tested the proton transfer reaction from the protonated surrounding residue Asp183 to the heme propionic group using QM/MM calculations (Figure S1). Our calculations show that the PT reaction is very endothermic (Figure S1), suggesting that the protonation of the surrounding residues is favored over the protonation at heme propionic groups. The general AMBER force field (GAFF)⁴² was used to model the dimeric lignin substrate and tartaric acid with the atomic charges assigned as the RESP charges⁴³ at the B3LYP/6-31G(d) level of theory. The force field parameters for Cpd I and the protonated Cpd II were generated using the MCPB.py program.^{44,45} The Amber ff14SB force field⁴⁶ was employed to simulate the protein. Finally, the system was solvated in a rectangular box of TIP3P waters, which extends to a minimum distance of 16 Å from the protein surface. Chloride/sodium ions were added to neutralize each system.

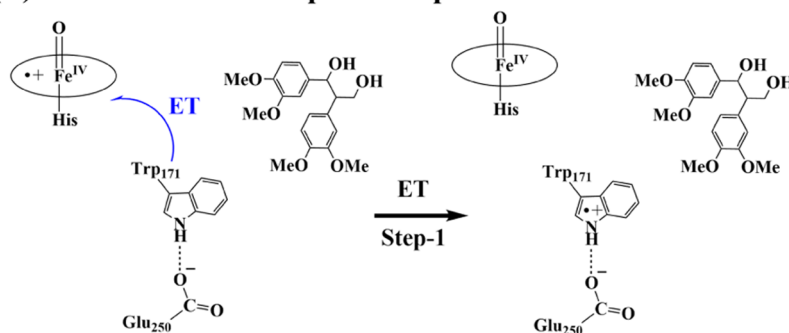
After proper setup, the system was minimized for 20,000 steps using the steepest descent algorithm, followed by 20,000 steps using the conjugate gradient algorithm. Then, the system was heated from 0 to 300 K in 50 ps under NVT ensemble with a weak restraint of 25 kcal/mol/Å² on the protein. To achieve a uniform density after heating, 1 ns of density equilibration was performed under the NPT ensemble, where the target temperature of 300 K was maintained using the Langevin thermostat⁴⁷ with a collision frequency of 2 ps, while the target pressure of 1.0 atm was controlled using the Berendsen barostat⁴⁸ with a pressure relaxation time of 1 ps. Afterward, a production MD simulation was propagated for 50 ns under the NPT ensemble. During the equilibration and production runs, a weak restraint of 25 kcal/mol/Å² has been applied to the substrate because the substrate binding is flexible at the enzyme–water interface. A 2 fs time-step was used for all of the MD runs. The SHAKE algorithm was used to constrain the covalent bonds involving hydrogen atoms, while the “three-point” SHAKE algorithm was used for the water molecules. All MD simulations were performed using the pmemd.cuda program in the Amber18 software package.⁴⁹

2.2. QM/MM MD Simulations

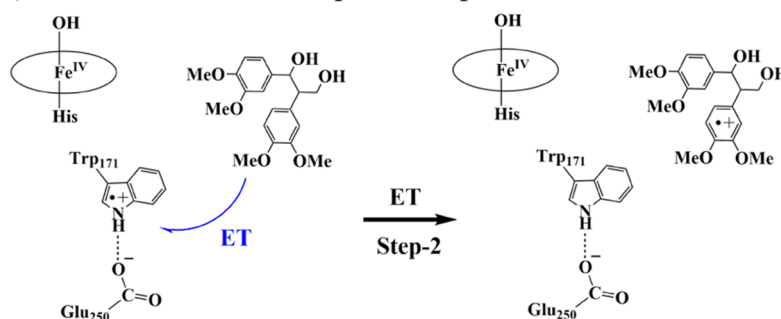
A representative snapshot between 40 and 50 ns of the production MD trajectory was used for the subsequent QM/MM MD simulations (see Figures S3 and S4). These selected structures are quite close to

Scheme 2. Three reaction steps involved in the one-electron oxidation of lignin by Cpd I in Stage II (see Scheme 1)

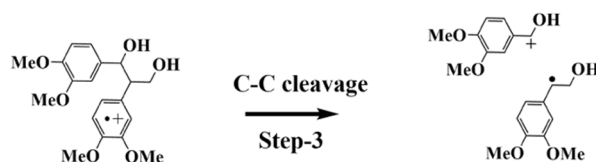
(A) The first ET from Trp171 to Cpd I



(B) The second ET from Trp171 to Cpd I



(C) The C-C cleavage of lignin cation radical



the most populated structures from the cluster analysis of the MD production trajectory (Figures S4–S9). All QM/MM Born–Oppenheimer MD simulations were performed using the CP2K 5.0 package,⁵⁰ along with the QM program QUICKSTEPS⁵¹ and the MM driver FIST. In this code, a real space multigrad technique is used to compute the electrostatic coupling between the QM and MM regions.^{52,53} The QM region was modeled at the DFT(UB3LYP-D3) level, employing the dual basis set formalism of Gaussian and plane waves (GPW),⁵¹ whereas the remaining part of the system was modeled at the MM level using the same parameters as in the classical MD simulations. For the QM calculations, the Gaussian double- ζ valence polarized (DZVP) basis set was used to expand the wave function,⁵⁴ while the auxiliary plane-wave basis set with a density cutoff of 360 Ry and GTH pseudopotentials⁵⁵ was utilized to converge the electron density. The dangling bonds between the QM and MM regions were capped with hydrogen atoms. The QM region consists of the electron donor, the electron acceptor, and the surrounding key residues, which have been specified for each step (see Figure S10). To speed up the calculation of Hartree–Fock exchange within the B3LYP hybrid functional, the auxiliary density matrix method (ADMM) was used.⁵⁶ All QM/MM MD simulations were performed under the NVT ensemble using a time step of 0.5 fs. The system was equilibrated without any constraints for 2 ps for the first ET step and 5 ps for the second ET step, respectively. For QM/MM metadynamics calculations, the width of the Gaussian hills was set to 0.2 Å, the Gaussian height was set to 0.6 kcal/mol, while the time deposition interval between the two consecutive Gaussians was set to 10 fs. In our study, one recrossing over the transition state, as recommended in literature studies, was taken as convergence criteria

for metadynamics calculations.⁵⁷ Our QM/MM calculated spin density population of Cpd I is provided in Figure S11, which corresponds to the typical electron state of Cpd I.⁵⁸ As discussed previously,⁵⁹ multireference and multiconfiguration (MR/MC) methods could possibly achieve better accuracy than DFT methods, but in practice, it is quite challenging to be used as MR/MC calculations require a very balanced treatment of electron correlation for a few states.⁵⁸

2.3. QM Model Calculations

All QM model calculations were performed using Gaussian 16 software.⁶⁰ The geometries of interested species were fully optimized in conjunction with the SMD continuum solvation model⁶¹ at the B3LYP-D3/def2-SVP level of theory.^{62–65} The energies were further refined with the larger basis set def2-TZVPP for all atoms.⁶⁴ Harmonic frequency calculations were performed at the same level of theory as the optimizations to estimate the zero-point energies as well as the thermal and entropic corrections. In addition, we also tested the ω B97XD functional for the calculation of the electronic coupling. With ω B97XD, the calculated electronic coupling for the second ET step is 0.015 eV, which is close to the value of 0.021 eV obtained by B3LYP. As QM-optimization may lead to the shortening of the donor–acceptor distance compared to the one within the protein environment, we have adjusted the electronic couplings based on the difference between the QM-optimized ET distance and the averaged ET distance from the QM/MM MD simulation (Eqs. 2 and 5 in SI).

2.4. Calculations of the ET and PCET Rates

The Marcus theory⁶⁶ was used to calculate the ET rates (eq 1). Herein, ΔG° is the reaction-free energy based on QM calculations. V_{el} is the electronic coupling calculated using the fragment charge difference (FCD) method⁶⁷ implemented in the Q-chem program⁶⁸ and by considering the distance correction. λ is the total reorganization energy, in which the inner-sphere reorganization energy was calculated using the four-point method, while the outer-sphere (or solvent) reorganization energy was calculated by using the two-sphere model.⁶⁹

$$k_{ET} = \frac{1}{\hbar} |V_{el}|^2 \sqrt{\frac{\pi}{\lambda k_B T}} \exp\left[-\frac{(\Delta G^\circ + \lambda)^2}{4\lambda k_B T}\right] \quad (1)$$

$$k_{PCET} = \frac{1}{\hbar} |V_{el}|^2 \sqrt{\frac{\pi}{\lambda k_B T}} \sum_{\mu} P_{\mu} \sum_{\nu} \langle |S_{\mu\nu}(R_{PT})|^2 \rangle \exp\left[-\frac{(\Delta G_{\mu\nu} + \lambda)^2}{4\lambda k_B T}\right] \quad (2)$$

The nonadiabatic PCET theory^{70–72} was used to calculate the PCET rate (eq 2). For the PCET calculations, the calculations of the electronic coupling follow the same protocol as for the ET reactions, while calculations of the reorganization energy follow a similar protocol as for the ET reactions. In eq 2, $\Delta G_{\mu\nu}$ means the reaction-free energy with the donor-proton in the vibrational state μ and the acceptor-proton in the vibrational state ν . P_{μ} is the Boltzmann population of the donor-proton in the vibrational state μ . $S_{\mu\nu}$ is the overlap integral between the donor-proton and acceptor-proton vibrational wavefunctions when they are in the states μ and ν , respectively. $S_{\mu\nu}$ is a function of R_{PT} , which is the donor–acceptor distance. Morse potentials were used to model the donor-proton and acceptor-proton vibrations. In the PCET calculations, the donor-hydrogen and acceptor-hydrogen vibrational states up to the third excited states (with $\mu_{max} = 3$ and $\nu_{max} = 3$) were taken into account to ensure the convergence. Further details about the calculations of the ET and PCET rates are shown in the SI.

3. RESULTS AND DISCUSSION

As summarized in Scheme 1, the whole catalytic cycle of LiP can be divided into three main stages. Among these stages, the activation of H_2O_2 (stage I), en route to the formation of Cpd I, can proceed via the well-established “Poulos–Kraut mechanism”.^{12,73} Such a mechanism via the heterolytic cleavage of the O–O bond has been extensively studied in heme-dependent metalloenzymes.^{74–79} As such, our study would focus on stage II in Scheme 1, which is comprised of two consecutive ET steps and the subsequent C–C cleavage of lignin cation radical (Scheme 2). The first ET step involves the long-range ET from Trp171 to Cpd I, generating the Trp171 radical and Cpd II. Due to the basicity of Cpd II and the acidic pH environment, Cpd II would undergo the facile protonation to form the Fe(IV)-OH species, i.e., the protonated Cpd II.^{13,80,81} The formation of the protonated Cpd II could inhibit the back ET from Cpd II to the Trp radical. The second ET step involves the long-range ET from the lignin substrate to the Trp171 radical, leading to the intact Trp171 residue and the lignin cation radical species. Then, the C–C cleavage can occur in the lignin cation radical species, leading to the lignin fragments.

In stage III, the protonated Cpd II would be responsible for the second-round substrate oxidation. As the reaction mechanism in stage III is expected to be similar to that in stage II, the present study focuses on stage II (Scheme 2), and the obtained insights can be transferred to stage III straightforwardly. In the following sections, we first performed

QM/MM MD simulations to track the plausible ET mechanism at pH = 7 and pH = 3. In particular, the state-of-the-art QM/MM MD simulations can enable us to obtain the equilibrated structures before/after the ET/PCET processes and to gauge the thermodynamics of the ET/PCET processes. However, as noted in our previous study,⁹³ the QM/MM MD simulations may significantly overestimate the rate of an ET reaction, mostly due to the neglect of the electronic transmission coefficient in the Marcus theory. Thus, the ET and PCET rate constants were later calculated with the nonadiabatic ET and PCET theories. Finally, the cluster-continuum model calculations were performed to investigate the C–C cleavage of the lignin cation radical in water solution.

3.1. Participation of pH Buffer in Catalysis

As we mentioned in the introduction, the condition at pH \sim 3 can speed up the lignin degradation by up to $\sim 10^3$ -fold when compared to that at the neutral pH condition (pH \sim 7). In experiments, the pH buffer of tartaric acid has been widely used in studies of LiP.^{82–84} Tartaric acid is a diprotic acid with two pK_a values of 3.0 and 4.3, respectively. Thus, diprotic acid would have at least one carboxyl group protonated at pH \sim 3. As an organic acid, tartaric acid can act as a proton donor or H-bonding donor to a plausible base. For residues surrounding Trp171, the predicted pK_a values are 4.11 for Asp264 and 2.94 for Glu250. Thus, Asp264 would be in the protonated form, while Glu250 is likely in the deprotonated form at pH \sim 3. As the deprotonated Glu250 is the only available base at the surface of LiP that is exposed to the solvent, the protonated carboxylic group of tartaric acid may form a H-bond to the deprotonated Glu250 (see Figure 2). To further investigate the effect of including the tartaric acid explicitly at pH = 3, we have investigated both ET steps at pH = 3 with or without tartaric acid.

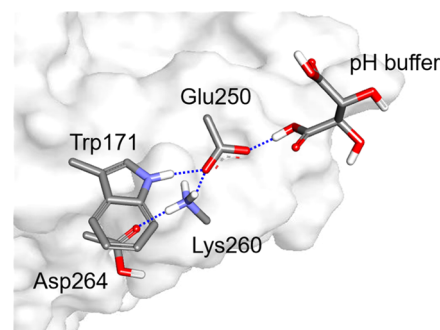


Figure 2. Local structure of Trp171 at pH = 3. Asp264 is protonated, while the surface-exposed Glu250 residue is available to form a H-bond with the pH buffer of tartaric acid.

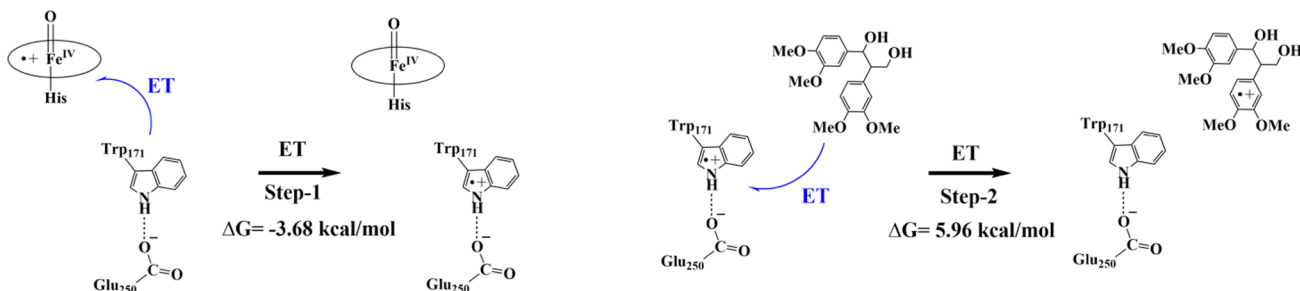
3.2. QM/MM MD Simulations of the Two ET Steps at pH = 7 and pH = 3

In Scheme 3, we present two ET steps at pH = 7 and pH = 3 (with tartaric acid). In addition, the QM-calculated reaction-free energy is shown for each ET step.

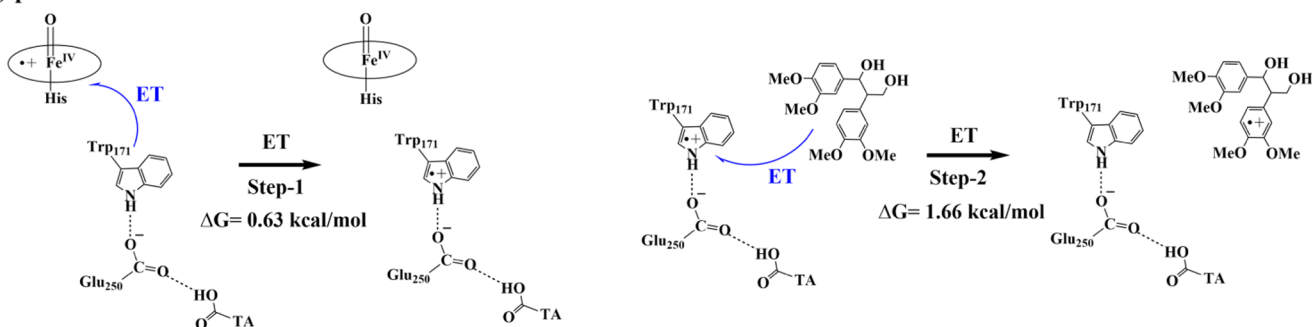
3.2.1. First ET from Trp171 to Cpd I at pH \sim 7. To decipher the mechanism of the first ET step from Trp171 to Cpd I at pH = 7, MD and QM/MM MD simulations have been carried out. First, our classical MD simulations indicated that the sidechain N atom of Trp171 keeps a distance of ~ 16.8 Å from the Fe atom in the heme group (see Figure S12). Such distance is reasonable for biological electron transfer.⁸⁵ Then,

Scheme 3. Illustration of Two ET Steps at pH = 7 and pH = 3, along with the QM-Calculated Reaction-Free Energy (in kcal/mol) for Each Step. At pH = 7, Asp264 is Deprotonated, while the pH Buffer of Tartaric Acid is Fully Deprotonated and is Not Able to Donate a H-Bond to Glu250. At pH = 3, Asp264 is Protonated, and the pH Buffer of Tartaric Acid is Able to Donate a H-Bond to Glu250

(A) pH=7



(B) pH=3



we calculated the ET pathway from the Trp171-N atom to the Heme-Fe atom using the Pathways plugin in VMD software.⁸⁶ As shown in Figure 3, the most favorable ET pathway between

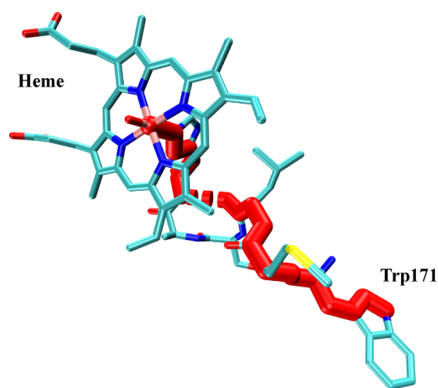


Figure 3. Most favorable ET pathway from Trp171 to Cpd I.

these two atoms is Trp171 → Met172 → Leu173 → His176 → Heme. Based on the representative structure from the classical MD simulations, we carried out the QM/MM MD simulations, in which the key residues along the ET pathway were included in the QM region.

Our QM/MM MD simulation shows that an electron can transfer from Trp171 to Cpd I within ~220 fs (Figure S13), affording the Trp171-H^{•+} cation radical (Figure 4). This finding suggests that the first ET step is favorable thermodynamically, which is consistent with our QM model calculations (with an exergonicity of 3.68 kcal/mol, see Scheme 3). In addition, this result suggests that the long-range ET from Trp171 to Cpd I follows an outer-sphere ET

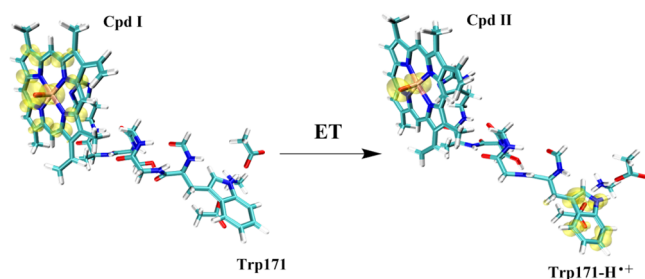


Figure 4. Evolution of the spin density distribution during the first ET step (Trp171 → Cpd I) at pH = 7 during the QM/MM MD simulations.

mechanism rather than a PCET mechanism, as the ET was not coupled to the proton transfer from Trp171 to Glu250.

3.2.2. Second ET from the Lignin Substrate to Trp171 at pH ~ 7. In the last section, our QM/MM MD simulations suggest that the ET from Trp171 to Cpd I follows an outer-sphere ET mechanism, yielding the Trp171-H^{•+} cation radical and Cpd II. Then, Cpd II would undergo a fast protonation to form the Fe(IV)-OH species (i.e., the protonated Cpd II), while the Trp171-H^{•+} cation radical would oxidize the lignin substrate either via an outer-sphere ET mechanism or via a PCET mechanism. Unlike the first ET step, we did not observe a spontaneous ET from the lignin substrate to the Trp171-H^{•+} cation radical during 5 ps QM/MM MD simulation (Figure S14), suggesting that the second ET step at pH = 7 may be unfavorable thermodynamically. This agrees with our QM model calculations, which showed that the second ET is endergonic by 5.96 kcal/mol at pH = 7 (see Scheme 3).

Next, we have investigated the proton transfer (PT) from the Trp171-H^{•+} cation radical to Glu250 using QM/MM

metadynamics simulations (Figure 5). It is seen that such a PT reaction is accessible both thermodynamically and kinetically,

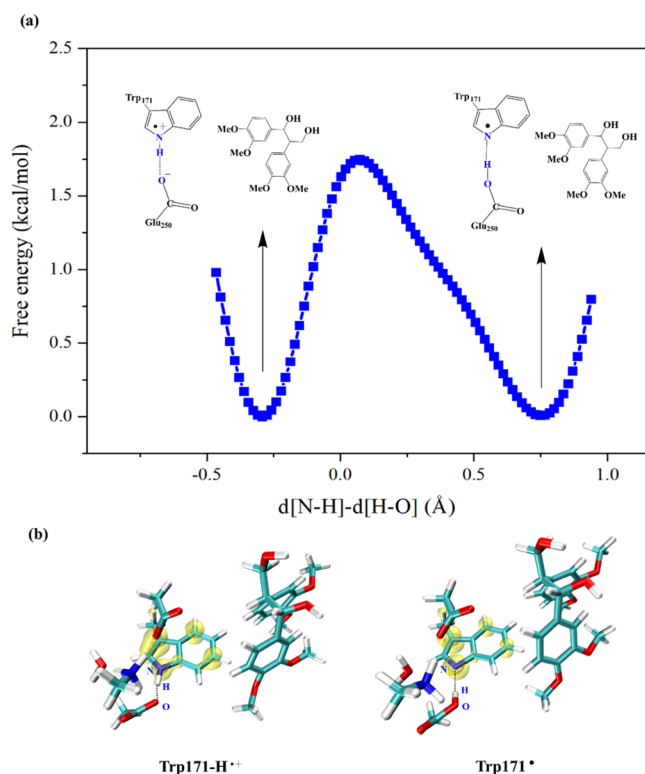


Figure 5. (a) Free energy profile for the PT from the Trp171-H^{•+} cation radical to Glu250 calculated by the QM/MM metadynamics simulations. The reaction coordinate was defined as the difference between the N–H distance and O–H distance, with the three atoms marked by blue color. (b) Representative structures of the QM region in the reactant and product states of the PT reaction, where the spin-up isodensity surfaces are depicted in yellow.

leading to a Trp171[•] neutral radical species. In addition, the Trp171-H^{•+} cation radical form has similar free energies with the Trp171[•] neutral radical form, suggesting that these two forms may coexist at pH = 7. If we inspect the reverse PT reaction from Glu250 to Trp171, we found the PT could not drive the ET from the lignin substrate to the Trp171[•] radical, suggesting that the concerted PCET mechanism is not favorable. In the latter section, both the ET and PCET rates were calculated and compared using the nonadiabatic ET/PCET theory.

3.2.3. First ET from Trp171 to Cpd I at pH ~ 3 without Tartaric Acid. We also performed QM/MM MD simulations of the system at pH ~ 3. First, we have investigated the first ET step at pH ~ 3 without tartaric acid. QM/MM MD simulation shows a spontaneous electron transfer from Trp171 to Cpd I within ~300 fs (Figure S13), leading to the Trp171-H^{•+} cation radical. This is consistent with our QM model calculations, showing that the first ET step, which generates a Trp171-H^{•+} cation radical, is exergonic by 1.11 kcal/mol (see Figure S16). Moreover, further QM/MM MD simulation led to a spontaneous PT from the Trp171-H^{•+} cation radical to Glu250 within ~620 fs, yielding a Trp171[•] neutral radical and the protonated Glu250 (see Figure 6). This result suggests that PT from the Trp171-H^{•+} cation radical to Glu250 is favorable thermodynamically at pH ~ 3 without tartaric acid.

3.2.4. Second ET from the Lignin Substrate to Trp171 at pH ~ 3 without Tartaric Acid. In the last section, our QM/MM MD simulations suggest that the first ET step at pH ~ 3 without tartaric acid follows a stepwise ETPT mechanism, yielding a Trp171[•] neutral radical and Cpd II. Unlike the first ET step, we did not observe a spontaneous ET from the lignin substrate to the Trp171[•] neutral radical during the 5 ps QM/MM MD simulation (Figure S14), suggesting that the Trp171[•] neutral radical is inefficient for mediating the ET process. As the protonated Glu250 forms a persistent H-bond with Trp171 during QM/MM simulations, we assume that it may back donate the proton to the Trp171 neutral radical, which may drive the long-range ET from the lignin substrate to the Trp171[•] neutral radical via a PCET mechanism. To verify such a possibility, QM/MM metadynamics simulations were carried out to study the thermodynamics of this PCET process, with the calculated free energy profile depicted in Figure 7. It was seen that the PT from Glu250 to the Trp171[•] neutral radical is coupled with the ET from the lignin substrate to the Trp171[•] neutral radical, yielding an intact Trp171 and a lignin cation radical. This process involves a free energy barrier of ~7.5 kcal/mol and a free energy change of ~2 kcal/mol. Compared to the case at pH = 7, the protonation of Asp264 at pH = 3 may increase the redox potential of the Trp171[•] neutral radical, which makes the PCET accessible thermodynamically.

3.2.5. First ET from Trp171 to Cpd I at pH ~ 3 with Tartaric Acid. At pH = 3, we assume that the tartaric acid buffer would form a strong H-bond with the surface-exposed deprotonated Glu250. To test such possibility, a tartaric acid molecule was docked into the proximity of Glu250 (Figure S18), based on which we carried out the classical MD and QM/MM MD simulations. Our QM/MM MD simulations

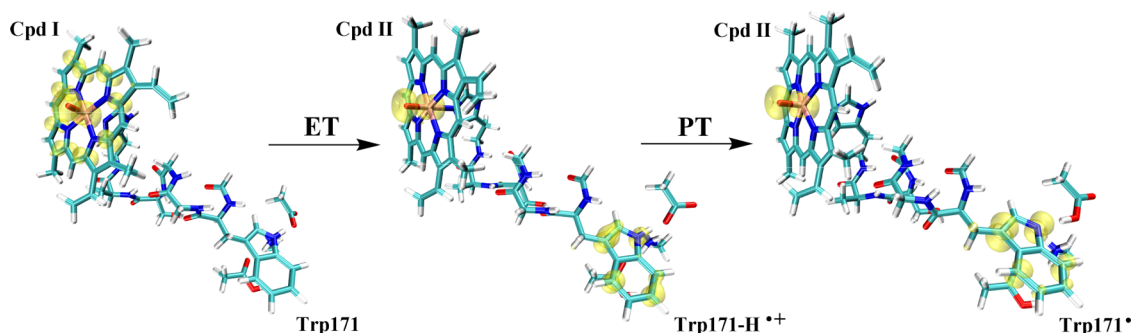


Figure 6. Evolution of the spin density distribution during the first ET step (Trp171 → Cpd I) at pH ~ 3 without tartaric acid during the QM/MM MD simulations.

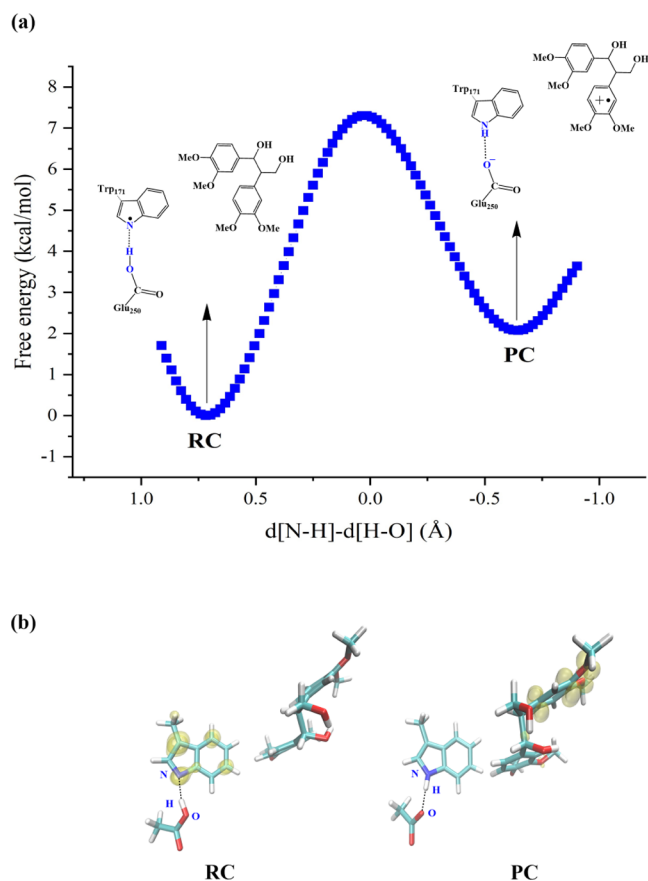


Figure 7. (a) Free energy profile for the second ET step via a PCET mechanism at pH \sim 3 without tartaric acid calculated by the QM/MM metadynamics simulations. The reaction coordinate was defined as the difference between the N–H distance and O–H distance, with the three atoms marked by the blue color. RC means the reactant complex, while PC means the product complex. (b) Representative structures of the QM region in the reactant and product states, where the spin-up isodensity surfaces are depicted in yellow.

indicated that the tartaric acid molecule could form a persistent and strong H-bond with Glu250, with an average O–H distance of 1.69 Å (Figure S19). Similar to the case without tartaric acid at pH = 3, our QM/MM MD simulation showed a spontaneous ET from Trp171 to Cpd I (Figure S13), which yielded Cpd II and the Trp171-H^{•+} cation radical. This can be confirmed by the spin density accumulation in Trp171 after the ET (see Figure 8). In addition, QM/MM MD simulations show that the ET process can be crossed back (Figure S13), suggesting that the first ET step with tartaric acid is almost thermally neutral, which is in line with the QM-calculated value of 0.63 kcal/mol for the reaction free energy (Scheme 3).

Unlike the one without tartaric acid at pH = 3, we did not observe the spontaneous PT from the Trp171-H^{•+} cation radical to Glu250 during QM/MM MD simulations, suggesting that the presence of a strong H-bond with tartaric acid can significantly undermine the basicity of Glu250 for proton reception. This observation agrees with our QM calculations (Figure S20), showing that this step is endergonic by 3.8 kcal/mol. Thus, our simulations suggest that the first ET step transpires via a pure ET mechanism in the presence of tartaric acid. In addition, the presence of tartaric acid can inhibit the PT from the Trp171-H^{•+} cation radical to Glu250,

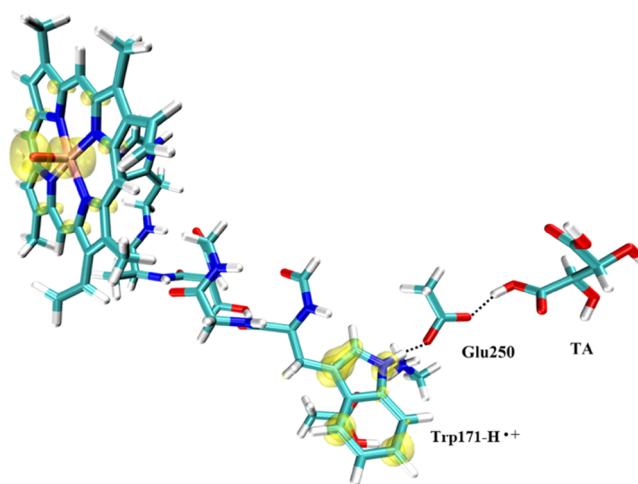


Figure 8. Spin density distribution of heme and Trp171 after the first ET step at pH \sim 3 with tartaric acid from the QM/MM MD simulations.

which thus stabilizes the Trp171-H^{•+} cation radical and inhibits the formation of the Trp171[•] neutral radical.

The pK_a of Glu250 is \sim 2.94, suggesting that it is mostly in the deprotonated state at pH = 3. This is consistent with our QM/MM MD simulations, showing that the proton stays dominantly on tartaric acid rather than on Glu250 at pH = 3. For comparison, we also performed MD simulations for the Glu250-protonated state at pH = 3 (without tartaric acid). The MD simulations show that the protonated Glu250 would move far away from Trp171, as the protonated Glu250 cannot be strongly H-bonded to the positively charged Lys260 (Figure S21). In addition, without the deprotonated Glu250, our QM model calculations show that the electron affinity of the Trp171-H^{•+} cation radical would increase by 5.6 kcal/mol (Figure S22), which would be highly unfavorable for the first ET. Thus, there exists a minor possibility that Glu250 would be protonated. These findings also rationalize why the Trp-Glu pair is conserved in all lignin peroxidases (Figure S23).

3.2.6. Second ET from the Lignin Substrate to Trp171 at pH \sim 3 with Tartaric Acid. Again, we found that tartaric acid could form a persistent and strong H-bond with Glu250, with an average O–H distance of 1.51 Å (see Figure S24). Unlike the one without tartaric acid, we observed a spontaneous ET from the lignin substrate to the Trp171-H^{•+} cation radical in the presence of tartaric acid, which yielded the lignin cation radical and the intact Trp171 (Figure 9). Such a finding implies that the formation of the strong H-bond between Glu250 and tartaric acid can significantly facilitate the thermodynamics for the second ET step. Such a finding is in line with our QM model calculations (Scheme 3), showing that pH \sim 3 with tartaric acid can facilitate the thermodynamics of the second ET by 4.3 kcal/mol compared to that at pH = 7.

3.2.7. Reaction Rates Calculated Based on the Nonadiabatic ET or PCET Theories. Because the QM/MM MD simulations may significantly underestimate the barriers of a nonadiabatic ET or PCET process due to the neglect of the electronic or vibronic transmission coefficient, the reaction rates of the nonadiabatic ET and PCET reactions were evaluated by the nonadiabatic ET and PCET theories. Table 1 shows the calculated rate constants for two ET steps at pH = 7 (without tartaric acid) and pH = 3 (with tartaric acid), respectively. As indicated by our

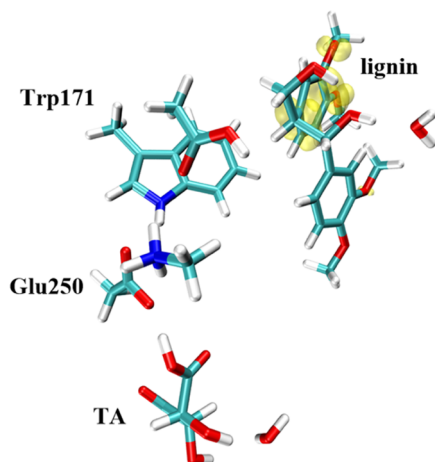


Figure 9. Spin density distribution of Trp171 and the lignin substrate after the second ET step at pH \sim 3 with tartaric acid from the QM/MM MD simulations.

Table 1. Calculated ET and PCET Rates According to the Marcus Theory and Nonadiabatic PCET Theory^a

	pH = 7 (without tartaric acid)		pH = 3 (with tartaric acid)	
	step-1	step-2	step-1	step-2
k_{ET} (s^{-1})	4.8×10^3	9.3×10^4	9.6×10^2	1.3×10^7
k_{PCET} (s^{-1})	N/A	9.0^b	N/A	N/A

^aThe parameters for these calculations are shown in Tables S2 and S3.

^bAs our QM/MM MD simulations suggest that the PT from the Trp171-H^{•+} cation radical to Glu250 is nearly thermoneutral, the driving force of the PCET is approximated to be the same as that of the ET.

simulations (Section 3.2), the second ET step at pH = 7 is inaccessible, while all of the other ET reactions follow an outer-sphere ET mechanism. As such, the ET rates have been calculated for all of the steps. For the second ET step at pH = 7, both the ET and PCET rates have been calculated for the second ET step at pH = 7, given that the Trp171-H^{•+} cation radical and the neutral radical can coexist under such conditions. Table 1 summarizes the nonadiabatic ET or PCET rate constants, while the parameters for these calculations are provided in Tables S2–S3.

We can see: (1) for both pH = 7 and pH = 3, the second ET step shows a much faster reaction rate than that in the first ET step; this is mainly because the calculated electronic coupling in the second ET step (\sim 0.02 eV) is much higher than that in the first ET step (\sim 0.00024 eV); (2) the low pH condition (pH = 3) slightly reduces the rate of the first ET step but significantly increases the rate of the second ET step; (3) for the second ET step at pH = 7, the calculated ET rate is \sim 4 orders higher than the PCET rate, this is mainly because the Trp171-H^{•+} cation radical is an accessible intermediate that is as stable as the Trp171[•] neutral radical (see Figure 5). In such a case, the ET pathway can be remarkably favorable over the concerted PCET pathway.² (4) The calculated ET rate is about two orders of magnitude higher than the catalytic rate for lignin degradation at pH = 3,³³ while it is about five orders of magnitude higher than the catalytic rate for lignin degradation at pH = 7,³³ suggesting that the two ET steps may not be the rate-determining step in the catalytic cycle.

3.2.8. How pH Buffer Accelerates the Degradation of the Lignin Substrate. As indicated in Scheme 1, the reactions in stage II consist of two consecutive ET steps and the subsequent C–C cleavage of the lignin cation radical (Scheme 2). Thus, we proceed to investigate the water-mediated decomposition of the lignin cation radical with hybrid cluster-continuum (HCC) model calculations.^{87,88} Our calculations showed that the C–C cleavage of the lignin cation radical, which is coupled to the proton transfer to the surrounding waters, involves a free energy barrier of 13.8 kcal/mol (Figure S27).

For the first ET step at either pH \sim 7 or pH \sim 3, our QM/MM MD have shown the spontaneous electron transfer from Trp171 to Cpd I, suggesting that the reaction-free energy (ΔG) of this step is less than or close to 0 kcal/mol. For the second ET step, our QM/MM MD simulations have shown that pH \sim 3 with tartaric acid can significantly facilitate ET from lignin to the Trp171-H^{•+} cation radical. Indeed, QM calculations have shown that the second ET is endergonic by 5.96 kcal/mol at pH \sim 7 without tartaric acid, while the reaction is endergonic by only 1.66 kcal/mol at pH \sim 3 with tartaric acid. Thus, the condition of pH \sim 3 with tartaric acid can reduce the endergonicity of the second ET by \sim 4.3 kcal/mol.

With these values in hand, we can map the energy profiles for LiP-catalyzed degradation of the lignin substrate at pH = 7

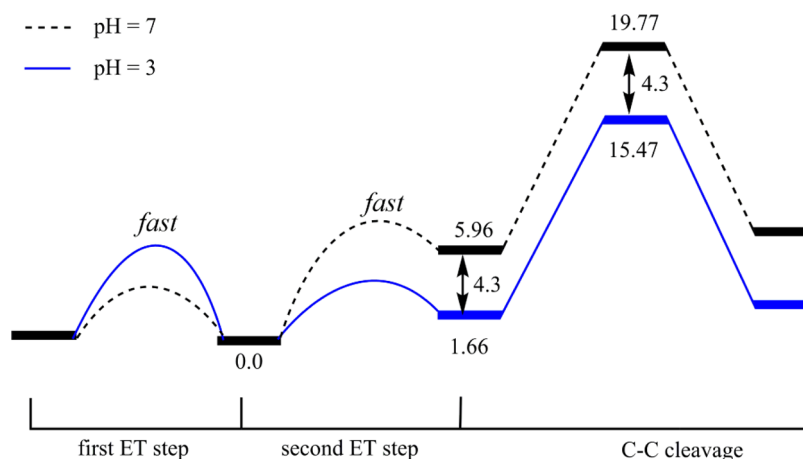


Figure 10. Comparison of the free energy profiles (in kcal/mol) for the degradation of the lignin substrate when at pH = 7 and pH = 3.

vs pH = 3 (Figure 10). As our nonadiabatic ET calculations showed, both ET steps are relatively fast, and the rate-limiting step would be the third step of the C–C cleavage of the lignin cation radical. As shown in Figure 10, the C–C cleavage has an overall barrier of 19.77 kcal/mol at pH = 7, while at pH = 3, the barrier has reduced to 15.47 kcal/mol. Notably, such reduction of barrier originated from the decreased endergonicity from the second ET step. According to the transition state theory, the reduction of the barrier of ~ 4.3 kcal/mol can lead to the rate enhancement of ~ 1480 -fold, which qualitatively agrees with the experimental observation that the decrease of pH from 7.39 to 3.06 can speed up the catalysis by 3 orders of magnitude.³³

3.2.9. Why pH Buffer can Enhance the Oxidizing Power of the Trp171-H^{•+} Cation Radical for Lignin Oxidation. At either pH = 7 or pH = 3, our QM/MM MD simulations have shown that the first ET step from Trp171 to Cpd I is spontaneous, suggesting that the increase of the redox potential of Cpd I at pH ~ 3 is not the key reason for the enhanced activity of LiP. To gain some clues on this, we have analyzed the intrinsic electric field (IEF) along the Fe–O bond from the MD trajectory of LiP–Cpd I at pH = 7 vs pH ~ 3 . Existing studies have shown that the IEF along the Fe–O bond has significant effects on the reactivity and redox potential of the Heme–Cpd I species.⁸⁹ For pH = 7, the calculated average IEF value is -72 MV/cm (Figure S28). Such a negative value suggests that the redox potential of Cpd I is intrinsically inhibited by the protein environment of LiP.⁹⁰ For pH = 3, the calculated average IEF value is -59 MV/cm (Figure S28), suggesting that the condition at pH = 3 can increase the redox potential of Cpd I compared to that at pH = 7. However, such elevation is not significant ($-72 \rightarrow -59$ MV/cm). Such a finding is in line with our QM/MM MD simulations, showing that the first ET step does not have much dependence on the pH conditions (Section 3.2.1 vs Section 3.2.5). Especially, the first ET step is spontaneous at both pH = 7 and pH = 3.

To understand how pH ~ 3 can increase the redox potential of the Trp171-H^{•+} cation radical by 4.3 kcal/mol relative to that at pH = 7, we have gauged the separate contributions of tartaric acid and the titratable residues close to Trp171. For pH = 3, our QM/MM MD simulations show that the formation of the H-bond between tartaric acid and Glu250 can significantly undermine the H-bonding strength between Glu250 and the Trp171 cation radical (Figure S29), which thus can increase the electron affinity of the Trp171 cation radical by ~ 1.7 kcal/mol (Figures 11a vs 11b). Such finding is

evident from the QM model calculations, showing that the replacement of tartaric acid by solvent water can decrease the accumulation of positive charge on the Trp171 cation radical (Mulliken charge of $+0.824e$ with tartaric acid in Figure 11a vs $+0.741e$ with water in Figure 11b).

Besides tartaric acid, we note that the titratable residue of Asp264, which forms a salt bridge with Lys260 and is just located above Trp171, can have significant effects on the redox potential of the Trp171-H^{•+} cation radical as well. The predicted pK_a value of Asp264 is 4.11, indicating that Asp264 is protonated at pH ~ 3 and deprotonated at pH ~ 7 . As shown in Figure 11, the electron affinity of the Trp171-H^{•+} cation radical with the protonated Asp264 (Figure 11a) is ~ 1.9 kcal/mol higher than that with the deprotonated Asp264 (Figure 11c). It is reasonable as the negatively charged Asp264 would decrease the electron affinity of the Trp171-H^{•+} cation radical. This is also supported by the accumulated positive charge on Trp171 ($+0.824e$ with the protonated Asp264 in Figure 11a vs $+0.784e$ with the deprotonated Asp264 in Figure 11c).

Obviously, the increased redox potential of the Trp171-H^{•+} cation radical at pH = 3 mainly originated from the protonation of Asp264 and the H-bonding formation between Glu250 and tartaric acid. Notably, except for the role of enhancing the redox potential of the Trp171-H^{•+} cation radical, tartaric acid also plays a key role in stabilizing the Trp171-H^{•+} cation radical. As demonstrated from our QM/MM metadynamics simulations, the absence of the strong H-bond from tartaric acid to Glu250 at pH ~ 7 could lead to the ultimate PT from the Trp171-H^{•+} cation radical to Glu250, affording the Trp171[•] neutral radical. As the Trp171[•] neutral radical can only oxidize the lignin substrate via a PCET mechanism and the calculated PCET rate is much lower than the calculated ET rate, the formation of the neutral Trp171[•] neutral radical would slow down the lignin oxidation. Thus, tartaric acid plays dual roles in modulating the reactivity of the Trp171-H^{•+} cation radical—it not only inhibits the PT from the Trp171-H^{•+} cation radical to Glu250, thereby stabilizing the Trp171 cation radical but also significantly enhances the redox potential of the Trp171-H^{•+} cation radical for the lignin oxidation.

In addition to tartaric acid, other weak acids such as citric acid, succinic acid, phosphoric acid, and acetic acid (Scheme 4) can be used in LiP experiments. For all of these pH buffers, at least one of the acid sites has a pK_a value higher than 3, suggesting that all of these weak acids can function as the H-bonding donor to Glu250 at pH = 3. Thus, the present finding can be generalized for different kinds of pH buffers.

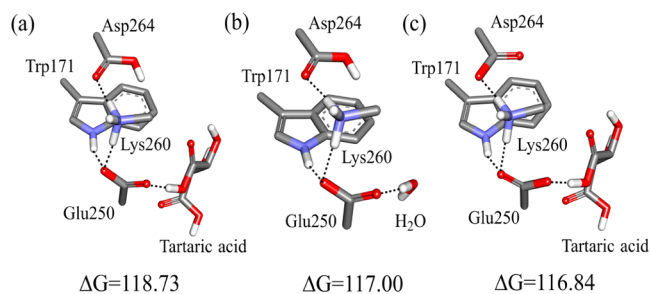
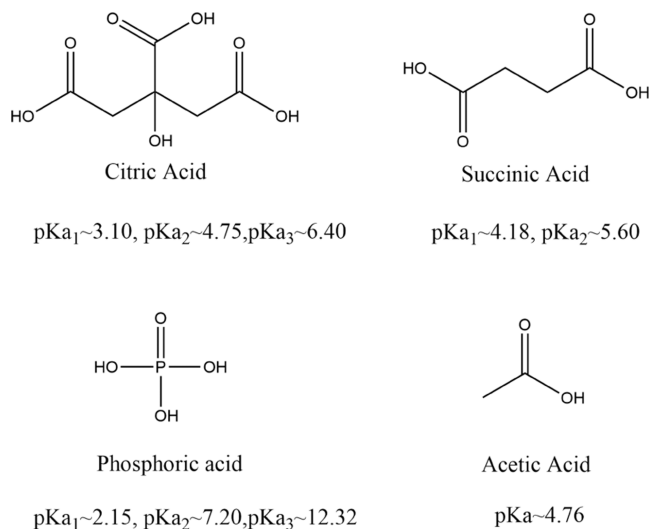


Figure 11. Calculated electron affinity (in kcal/mol) for the Trp171-H^{•+} cation radical with different environments. (a) Asp264 is protonated, while Glu250 is H-bonded to tartaric acid. (b) Asp264 is protonated, while Glu250 is H-bonded to solvent water. (c) Asp264 is deprotonated, while Glu250 is H-bonded to tartaric acid.

4. DISCUSSION AND CONCLUSIONS

In this work, we studied the pH-dependent degradation of lignin by lignin peroxidase using the QM/MM MD simulations and nonadiabatic ET/PCET theories. Upon the formation of Cpd I, the first-round degradation of lignin involves two successive ET steps and the subsequent C–C cleavage of the lignin cation radical. For both pH = 7 and pH = 3, our QM/MM MD simulations led to the spontaneous ET from Trp171 to Cpd I, affording the Trp171-H^{•+} cation radical. For pH = 3 without the pH buffer of tartaric acid, our QM/MM MD simulations led to the spontaneous proton transfer from the Trp171-H^{•+} cation radical to Glu250, yielding the Trp171[•] neutral radical species. Importantly, the presence of the second-sphere H-bond between Glu250 and tartaric acid at

Scheme 4. Various pH Buffers Used in Catalysis of LiPs



pH = 3 can inhibit the PT from the Trp171-H^{•+} cation radical to Glu250, thereby stabilizing the Trp171-H^{•+} cation radical. For the second ET step at pH = 7, a spontaneous ET from the lignin substrate to the Trp171-H^{•+} cation radical was not observed during the QM/MM MD simulations, suggesting that the second ET step is unfavorable thermodynamically, which can be supported by an endergonicity of 5.96 kcal/mol from QM model calculations. Importantly, the condition of pH = 3 with tartaric acid can greatly facilitate the thermodynamics of the second ET step by ~ 4.3 kcal/mol, leading to a spontaneous ET from the lignin substrate to the Trp171-H^{•+} cation radical as observed in QM/MM MD simulations.

Using the nonadiabatic ET/PCET theories, we have calculated the ET rates for both ET steps at pH = 7 and pH = 3. Our calculations show that both ET steps are relatively fast at pH = 7 and pH = 3. Moreover, for the second ET step at pH = 7, the calculated PCET rate is ~ 4 orders of magnitude smaller than the calculated ET rate, indicating the concerted PCET reaction is much slower than the corresponding ET reaction. Based on the calculated kinetics and thermodynamics

for the two ET steps and the subsequent C–C cleavage of lignin cation radical species, we have identified the root cause for the accelerated lignin degradation at pH = 3 relative to that at pH = 7. We found that the accelerated lignin degradation at pH = 3 mainly originated from the reduction of endergonicity in the second ET step. At pH = 3, the endergonicity of the second ET step can be reduced by ~ 4.3 kcal/mol relative to that at pH = 7. Accordingly, the overall barrier of the lignin oxidation can be reduced by 4.3 kcal/mol, which corresponds to a rate acceleration of ~ 3 orders of magnitude. This qualitatively agrees with the experimental observation.³³

In LiP, we have shown that pH buffer can modulate the redox potential of the Trp171-H^{•+} cation radical by functioning as both the proton donor and H-bond donor. As a H-bond donor to Glu250, tartaric acid can not only enhance the oxidizing power of the Trp171-H^{•+} cation radical but also inhibit the PT from the Trp171-H^{•+} cation radical to Glu250, thereby stabilizing the Trp171-H^{•+} cation radical intermediate for the one-electron oxidation of lignin substrate. For Asp264 located above Trp171, the protonation of Asp264 at pH = 3 can also effectively enhance the oxidizing power of the Trp171-H^{•+} cation radical. Notably, our calculations show that the Trp171-H^{•+}-mediated ET rate is much higher than the Trp171[•] radical-mediated PCET rate, indicating that the ET pathway is favored over the concerted PCET pathway.

These findings should have far-reaching implications for biological ET reactions. For instance, the redox-active residues, especially Tyr and Trp,^{91,92} are widely involved in biologically important proteins such as PSII,^{1,2,93–96} Ribonucleotide reductase (RNR),^{97–99} LPMO,^{100,101} and peroxidases.^{99,102,103} In these proteins, the redox-active Tyr or Trp residues usually have H-bonding interactions with adjacent basic residues (e.g., Asp, Glu, His). In such cases, the adjacent base may mediate the ET/PCET process or stabilize the cation radical intermediate via H-bonding interactions.^{30,104–106} Such a regulation would depend on the pK_a of redox-active residues. Specifically, for Trp, the experimentally characterized pK_a of the Trp171-H^{•+} cation radical is ~ 4.5 ,¹⁰⁷ suggesting that the adjacent base with a pK_a lower than 4.5 can stabilize the Trp171-H^{•+} cation radical for long-range ET reactions. As

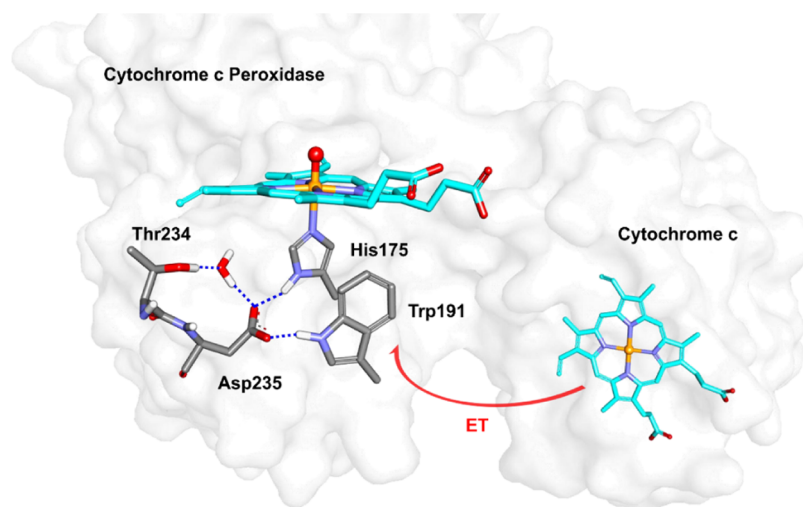


Figure 12. Second-sphere H-bonding interaction between Asp235 and His175 in cytochrome *c* peroxidase (CcP). This interaction may well stabilize the active site Trp191-H^{•+} cation radical, which could significantly accelerate the long-range ET from Cytochrome *c* to the active site of CcP.

demonstrated in our study, the second-sphere H-bonding interactions, either with acid buffers or other second-sphere residues, could significantly reduce the basicity of Glu250, thereby stabilizing the Trp171-H^{•+} cation radical for the lignin oxidation. Another representative example is cytochrome *c* peroxidase (see Figure 12), in which the second-sphere H-bonding interaction between Asp235 and His175 may well stabilize the active site Trp191-H^{•+} cation radical for accelerating the long-range ET from Cytochrome *c* to the active site of CcP.^{12,108} We expect that pH buffer could effectively regulate the redox properties of the redox-active residues via both the protonation of their proximal residues and the second-sphere H-bonding interactions, especially for redox-active residues exposed to solvents.

In sum, our study revealed the mechanistic basis for the pH buffer-accelerated lignin degradation by lignin peroxidase. The obtained knowledge could not only benefit the manipulation of biological ET reactions via engineering the second-sphere residues but also provide guidance for the relevant catalyst designs in the long run.

■ ASSOCIATED CONTENT

SI Supporting Information

The Supporting Information is available free of charge at <https://pubs.acs.org/doi/10.1021/jacsau.2c00649>.

Computational details; QM/MM MD results; QM-calculated free energy changes; and cartesian coordinates of all of the QM-computed species (PDF)

■ AUTHOR INFORMATION

Corresponding Authors

Pengfei Li – Department of Chemistry and Biochemistry, Loyola University Chicago, Chicago, Illinois 60660, United States; orcid.org/0000-0002-2572-5935; Email: pli4@luc.edu

Binju Wang – State Key Laboratory of Physical Chemistry of Solid Surfaces and Fujian Provincial Key Laboratory of Theoretical and Computational Chemistry, College of Chemistry and Chemical Engineering and Innovation Laboratory for Sciences and Technologies of Energy Materials of Fujian Province (IKKEM), Xiamen University, Xiamen 361005, P. R. China; orcid.org/0000-0002-3353-9411; Email: wangbinju2018@xmu.edu.cn

Authors

Wenhan Fang – State Key Laboratory of Physical Chemistry of Solid Surfaces and Fujian Provincial Key Laboratory of Theoretical and Computational Chemistry, College of Chemistry and Chemical Engineering and Innovation Laboratory for Sciences and Technologies of Energy Materials of Fujian Province (IKKEM), Xiamen University, Xiamen 361005, P. R. China

Shishi Feng – State Key Laboratory of Physical Chemistry of Solid Surfaces and Fujian Provincial Key Laboratory of Theoretical and Computational Chemistry, College of Chemistry and Chemical Engineering and Innovation Laboratory for Sciences and Technologies of Energy Materials of Fujian Province (IKKEM), Xiamen University, Xiamen 361005, P. R. China

Zhihui Jiang – State Key Laboratory of Physical Chemistry of Solid Surfaces and Fujian Provincial Key Laboratory of Theoretical and Computational Chemistry, College of

Chemistry and Chemical Engineering and Innovation Laboratory for Sciences and Technologies of Energy Materials of Fujian Province (IKKEM), Xiamen University, Xiamen 361005, P. R. China

Wanzhen Liang – State Key Laboratory of Physical Chemistry of Solid Surfaces and Fujian Provincial Key Laboratory of Theoretical and Computational Chemistry, College of Chemistry and Chemical Engineering and Innovation Laboratory for Sciences and Technologies of Energy Materials of Fujian Province (IKKEM), Xiamen University, Xiamen 361005, P. R. China; orcid.org/0000-0002-5931-2901

Complete contact information is available at: <https://pubs.acs.org/doi/10.1021/jacsau.2c00649>

Notes

The authors declare no competing financial interest.

■ ACKNOWLEDGMENTS

This work was supported by the National Natural Science Foundation of China (to B.W., with grants No. 22122305, 22073077, and 22121001). This work was partly supported by the start-up funds from Loyola University Chicago (to P.L.). The authors also thank the anonymous reviewers for their constructive suggestions.

■ ABBREVIATIONS

LiP	lignin peroxidase
VP	versatile peroxidase
MnP	manganese peroxidase
PSII	photosystem II
LPMO	lytic polysaccharide monooxygenase
RNR	ribonucleotide reductase
MD	molecular dynamics
QM/MM	quantum mechanical/molecular mechanical
PCET	proton-coupled electron transfer
ET	electron transfer
PT	proton transfer

■ REFERENCES

- (1) Huynh, M. H. V.; Meyer, T. J. Proton-coupled electron transfer. *Chem. Rev.* **2007**, *107*, 5004–5064.
- (2) Weinberg, D. R.; Gagliardi, C. J.; Hull, J. F.; Murphy, C. F.; Kent, C. A.; Westlake, B. C.; Paul, A.; Ess, D. H.; McCafferty, D. G.; Meyer, T. J. Proton-coupled electron transfer. *Chem. Rev.* **2012**, *112*, 4016–4093.
- (3) Kirk, T. K.; Farrell, R. L. Enzymatic “combustion”: the microbial degradation of lignin. *Annu. Rev. Microbiol.* **1987**, *41*, 465–501.
- (4) Falade, A. O.; Nwodo, U. U.; Iweriebor, B. C.; Green, E.; Mabinya, L. V.; Okoh, A. I. Lignin peroxidase functionalities and prospective applications. *MicrobiologyOpen* **2017**, *6*, No. e00394.
- (5) Camarero, S.; Sarkar, S.; Ruiz-Dueñas, F. J.; Martínez, M. a. J. s.; Martínez, A. n. T. Description of a versatile peroxidase involved in the natural degradation of lignin that has both manganese peroxidase and lignin peroxidase substrate interaction sites. *J. Biol. Chem.* **1999**, *274* (1), 10324–10330, DOI: [10.1074/jbc.274.15.10324](https://doi.org/10.1074/jbc.274.15.10324).
- (6) Ruiz-Duenas, F. J.; Morales, M.; García, E.; Miki, Y.; Martínez, M. J.; Martínez, A. T. Substrate oxidation sites in versatile peroxidase and other basidiomycete peroxidases. *J. Exp. Bot.* **2009**, *60*, 441–452.
- (7) Hofrichter, M. Lignin conversion by manganese peroxidase (MnP). *Enzyme Microb. Technol.* **2002**, *30*, 454–466.
- (8) Martínez, A. T. Molecular biology and structure-function of lignin-degrading heme peroxidases. *Enzyme Microb. Technol.* **2002**, *30*, 425–444.

- (9) Chan, J. C.; Paice, M.; Zhang, X. Enzymatic oxidation of lignin: challenges and barriers toward practical applications. *ChemCatChem* **2020**, *12*, 401–425.
- (10) Singh, A. K.; Bilal, M.; Iqbal, H. M.; Raj, A. Lignin peroxidase in focus for catalytic elimination of contaminants-A critical review on recent progress and perspectives. *Int. J. Biol. Macromol.* **2021**, *177*, 58–82.
- (11) Abdel-Hamid, A. M.; Solbiati, J. O.; Cann, I. K. Insights into lignin degradation and its potential industrial applications. *Adv. Appl. Microbiol.* **2013**, *82*, 1–28.
- (12) Poulos, T. L. Heme enzyme structure and function. *Chem. Rev.* **2014**, *114*, 3919–3962.
- (13) Huang, X.; Groves, J. T. Oxygen activation and radical transformations in heme proteins and metalloporphyrins. *Chem. Rev.* **2018**, *118*, 2491–2553.
- (14) Wong, D. W. S. Structure and action mechanism of ligninolytic enzymes. *Appl. Biochem. Biotechnol.* **2009**, *157*, 174–209.
- (15) Doyle, W. A.; Blodig, W.; Veitch, N. C.; Piontek, K.; Smith, A. T. Two substrate interaction sites in lignin peroxidase revealed by site-directed mutagenesis. *Biochemistry* **1998**, *37*, 15097–15105.
- (16) Hofrichter, M.; Ullrich, R.; Pecyna, M. J.; Liers, C.; Lundell, T. New and classic families of secreted fungal heme peroxidases. *Appl. Biochem. Biotechnol.* **2010**, *87*, 871–897.
- (17) Acebes, S.; Ruiz-Dueñas, F. J.; Toubes, M.; Sáez-Jiménez, V.; Pérez-Boada, M.; Lucas, M. F.; Martínez, A. T.; Guallar, V. Mapping the long-range electron transfer route in ligninolytic peroxidases. *J. Phys. Chem. B* **2017**, *121*, 3946–3954.
- (18) Blodig, W.; Doyle, W. A.; Smith, A. T.; Winterhalter, K.; Choinowski, T.; Piontek, K. Autocatalytic formation of a hydroxy group at C β of Trp171 in lignin peroxidase. *Biochemistry* **1998**, *37*, 8832–8838.
- (19) Johjima, T.; Wariishi, H.; Tanaka, H. Veratryl alcohol binding sites of lignin peroxidase from *Phanerochaete chrysosporium*. *J. Mol. Catal., B Enzym.* **2002**, *17*, 49–57.
- (20) Choinowski, T.; Blodig, W.; Winterhalter, K. H.; Piontek, K. The crystal structure of lignin peroxidase at 1.70 Å resolution reveals a hydroxy group on the C β of tryptophan 171: a novel radical site formed during the redox cycle. *J. Mol. Biol.* **1999**, *286*, 809–827.
- (21) Smith, A. T.; Doyle, W. A.; Dorlet, P.; Ivancich, A. Spectroscopic evidence for an engineered, catalytically active Trp radical that creates the unique reactivity of lignin peroxidase. *Proc. Natl. Acad. Sci. U.S.A.* **2009**, *106*, 16084–16089.
- (22) Blodig, W.; Smith, A. T.; Winterhalter, K.; Piontek, K. Evidence from spin-trapping for a transient radical on tryptophan residue 171 of lignin peroxidase. *Arch. Biochem. Biophys.* **1999**, *370*, 86–92.
- (23) Pérez-Boada, M.; Ruiz-Duenas, F. J.; Pogni, R.; Basosi, R.; Choinowski, T.; Martínez, M. J.; Piontek, K.; Martínez, A. T. Versatile peroxidase oxidation of high redox potential aromatic compounds: site-directed mutagenesis, spectroscopic and crystallographic investigation of three long-range electron transfer pathways. *J. Mol. Biol.* **2005**, *354*, 385–402.
- (24) Pogni, R.; Baratto, M. C.; Teutloff, C.; Giansanti, S.; Ruiz-Dueñas, F. J.; Choinowski, T.; Piontek, K.; Martínez, A. T.; Lenzian, F.; Basosi, R. A tryptophan neutral radical in the oxidized state of versatile peroxidase from *Pleurotus eryngii*: a combined multi-frequency EPR and density functional theory study. *J. Biol. Chem.* **2006**, *281*, 9517–9526.
- (25) Hammes-Schiffer, S.; Stuchebrukhov, A. A. Theory of coupled electron and proton transfer reactions. *Chem. Rev.* **2010**, *110*, 6939–6960.
- (26) Migliore, A.; Polizzi, N. F.; Therien, M. J.; Beratan, D. N. Biochemistry and theory of proton-coupled electron transfer. *Chem. Rev.* **2014**, *114*, 3381–3465.
- (27) Reinhardt, C. R.; Sayfutayrova, E. R.; Zhong, J.; Hammes-Schiffer, S. Glutamate Mediates Proton-Coupled Electron Transfer Between Tyrosines 730 and 731 in *Escherichia coli* Ribonucleotide Reductase. *J. Am. Chem. Soc.* **2021**, *143*, 6054–6059.
- (28) Barragan, A. M.; Soudackov, A. V.; Luthey-Schulten, Z.; Hammes-Schiffer, S.; Schulten, K.; Solov'ov, I. A. Theoretical Description of the Primary Proton-Coupled Electron Transfer Reaction in the Cytochrome bc 1 Complex. *J. Am. Chem. Soc.* **2021**, *143*, 715–723.
- (29) Berg, N.; Bergwinkl, S.; Nuernberger, P.; Horinek, D.; Gschwind, R. M. Extended Hydrogen Bond Networks for Effective Proton-Coupled Electron Transfer (PCET) Reactions: The Unexpected Role of Thiophenol and Its Acidic Channel in Photocatalytic Hydroamidations. *J. Am. Chem. Soc.* **2021**, *143*, 724–735.
- (30) Tyburski, R.; Liu, T.; Glover, S. D.; Hammarström, L. Proton-coupled electron transfer guidelines, fair and square. *J. Am. Chem. Soc.* **2021**, *143*, 560–576.
- (31) Shi, Q.; Pei, Z.; Song, J.; Li, S.-J.; Wei, D.; Coote, M. L.; Lan, Y. Diradical Generation via Relayed Proton-Coupled Electron Transfer. *J. Am. Chem. Soc.* **2022**, *144*, 3137–3145.
- (32) Nocera, D. G. Proton-Coupled Electron Transfer: The Engine of Energy Conversion and Storage. *J. Am. Chem. Soc.* **2022**, *144*, 1069–1081.
- (33) Marquez, L.; Wariishi, H.; Dunford, H. B.; Gold, M. H. Spectroscopic and kinetic properties of the oxidized intermediates of lignin peroxidase from *Phanerochaete chrysosporium*. *J. Biol. Chem.* **1988**, *263*, 10549–10552.
- (34) Castro, L.; Crawford, L. E.; Mutengwa, A.; Götze, J. P.; Bühl, M. Insights into structure and redox potential of lignin peroxidase from QM/MM calculations. *Org. Biomol. Chem.* **2016**, *14*, 2385–2389.
- (35) Blodig, W.; Smith, A. T.; Doyle, W. A.; Piontek, K. Crystal structures of pristine and oxidatively processed lignin peroxidase expressed in *Escherichia coli* and of the W171F variant that eliminates the redox active tryptophan 171. Implications for the reaction mechanism. *J. Mol. Biol.* **2001**, *305*, 851–861.
- (36) Trott, O.; Olson, A. J. AutoDock Vina: improving the speed and accuracy of docking with a new scoring function, efficient optimization, and multithreading. *J. Comput. Chem.* **2010**, *31*, 455–461.
- (37) Poulos, T. L.; Edwards, S. L.; Wariishi, H.; Gold, M. H. Crystallographic refinement of lignin peroxidase at 2 Å. *J. Mol. Biol.* **1993**, *268*, 4429–4440.
- (38) Pettersen, E. F.; Goddard, T. D.; Huang, C. C.; Couch, G. S.; Greenblatt, D. M.; Meng, E. C.; Ferrin, T. E. UCSF Chimera-a visualization system for exploratory research and analysis. *J. Comput. Chem.* **2004**, *25*, 1605–1612.
- (39) Sondergaard, C. R.; Olsson, M. H.; Rostkowski, M.; Jensen, J. H. Improved treatment of ligands and coupling effects in empirical calculation and rationalization of pKa values. *J. Chem. Theory Comput.* **2011**, *7*, 2284–2295.
- (40) Wallace, J. A.; Shen, J. K. Predicting pKa values with continuous constant pH molecular dynamics. *Methods Enzymol.* **2009**, *466*, 455–475.
- (41) Harris, R. C.; Shen, J. GPU-Accelerated Implementation of Continuous Constant pH Molecular Dynamics in Amber: pK(a) Predictions with Single-pH Simulations. *J. Chem. Inf. Model.* **2019**, *59*, 4821–4832.
- (42) Wang, J.; Merz, R. M.; Caldwell, J. W.; Kollman, P. A.; Case, D. A. Development and testing of a general amber force field. *J. Comput. Chem.* **2004**, *25*, 1157–1174.
- (43) Bayly, C. I.; Cieplak, P.; Cornell, W.; Kollman, P. A. A well-behaved electrostatic potential based method using charge restraints for deriving atomic charges: the RESP model. *J. Phys. Chem. A* **1993**, *97*, 10269–10280.
- (44) Li, P.; Merz, K. M. MCPB.py: A Python Based Metal Center Parameter Builder. *J. Chem. Inf. Model.* **2016**, *56*, 599–604.
- (45) Li, P.; Merz, K. M. Metal Ion Modeling Using Classical Mechanics. *Chem. Rev.* **2017**, *117*, 1564–1686.
- (46) Maier, J. A.; Martinez, C.; Kasavajhala, K.; Wickstrom, L.; Hauser, K. E.; Simmerling, C. ff14SB: improving the accuracy of protein side chain and backbone parameters from ff99SB. *J. Chem. Theory Comput.* **2015**, *11*, 3696–3713.

- (47) Izaguirre, J. A.; Catarello, D. P.; Wozniak, J. M.; Skeel, R. D. Langevin stabilization of molecular dynamics. *J. Chem. Phys.* **2001**, *114*, 2090–2098.
- (48) Berendsen, H. J. C.; Postma, J. P. M.; Gunsteren, W. F. v.; DiNola, A.; Haak, J. R. Molecular dynamics with coupling to an external bath. *J. Chem. Phys.* **1984**, *81*, 3684–3690.
- (49) Case, D. A.; Ben-Shalom, I. Y.; Brozell, S. R.; Cerutti, D. S.; Cheatham, T. E., III; Cruzeiro, V. W. D.; Darden, T. A.; Duke, R. E.; Ghoreishi, D.; Gilson, M. K.; Gohlke, H.; Goetz, A. W.; Greene, D.; Harris, R.; Homeyer, N.; Huang, Y.; Izadi, S.; Kovalenko, A.; Kurtzman, T.; Lee, T. S.; LeGrand, S.; Li, P.; Lin, C.; Liu, J.; Luchko, T.; Luo, R.; Mermelstein, D. J.; Merz, K. M.; Miao, Y.; Monard, G.; Nguyen, C.; Nguyen, H.; Omelyan, I.; Onufriev, A.; Pan, F.; Qi, R.; Roe, D. R.; Roitberg, A.; Sagui, C.; Schott-Verdugo, S.; Shen, J.; Simmerling, C. L.; Smith, J.; Salomon-Ferrer, R.; Swails, J.; Walker, R. C.; Wang, J.; Wei, H.; Wolf, R. M.; Wu, X.; Xiao, L.; York, D. M.; Kollman, P. A. AMBER2018, University of California, San Francisco.
- (50) CP2K version 5.0 (Development Version), the CP2K developers group. 2016. https://www.cp2k.org/version_history.
- (51) VandeVondele, J.; Krack, M.; Mohamed, F.; Parrinello, M.; Chassaing, T.; Hutter, J. Quickstep: Fast and accurate density functional calculations using a mixed Gaussian and plane waves approach. *Comput. Phys. Commun.* **2005**, *167*, 103–128.
- (52) Laino, T.; Mohamed, F.; Laio, A.; Parrinello, M. An efficient real space multigrid QM/MM electrostatic coupling. *J. Chem. Theory Comput.* **2005**, *1*, 1176–1184.
- (53) Laio, A.; VandeVondele, J.; Rothlisberger, U. A Hamiltonian electrostatic coupling scheme for hybrid Car–Parrinello molecular dynamics simulations. *J. Chem. Phys.* **2002**, *116*, 6941–6947.
- (54) VandeVondele, J.; Hutter, J. Gaussian basis sets for accurate calculations on molecular systems in gas and condensed phases. *J. Chem. Phys.* **2007**, *127*, No. 114105.
- (55) Goedecker, S.; Teter, M.; Hutter, J. Separable dual-space Gaussian pseudopotentials. *Phys. Rev. B* **1996**, *54*, 1703–1710.
- (56) Guidon, M.; Hutter, J.; VandeVondele, J. Auxiliary density matrix methods for Hartree–Fock exchange calculations. *J. Chem. Theory Comput.* **2010**, *6*, 2348–2364.
- (57) Ensing, B.; Laio, A.; Parrinello, M.; Klein, M. L. A recipe for the computation of the free energy barrier and the lowest free energy path of concerted reactions. *J. Phys. Chem. B* **2005**, *109*, 6676–6687.
- (58) Shaik, S.; Cohen, S.; Wang, Y.; Chen, H.; Kumar, D.; Thiel, W. P450 enzymes: their structure, reactivity, and selectivity-modeled by QM/MM calculations. *Chem. Rev.* **2010**, *110*, 949–1017.
- (59) Chen, H.; Lai, W.; Shaik, S. Multireference and multi-configuration ab initio methods in heme-related systems: what have we learned so far? *J. Phys. Chem. B* **2011**, *115*, 1727–1742.
- (60) Frisch, M. J.; Trucks, G. W.; Schlegel, H. B.; Scuseria, G. E.; Robb, M. A.; Cheeseman, J. R.; Scalmani, G.; Barone, V.; Petersson, G. A.; Nakatsuji, H.; Li, X.; Caricato, M.; Marenich, A. V.; Bloino, J.; Janesko, B. G.; Gomperts, R.; Mennucci, B.; Hratchian, H. P.; Ortiz, J. V.; Izmaylov, A. F.; Sonnenberg, J. L.; Williams, Ding, F.; Lipparini, F.; Egidi, F.; Goings, J.; Peng, B.; Petrone, A.; Henderson, T.; Ranasinghe, D.; Zakrzewski, V. G.; Gao, J.; Rega, N.; Zheng, G.; Liang, W.; Hada, M.; Ehara, M.; Toyota, K.; Fukuda, R.; Hasegawa, J.; Ishida, M.; Nakajima, T.; Honda, Y.; Kitao, O.; Nakai, H.; Vreven, T.; Throssell, K.; Montgomery, J. A., Jr.; Peralta, J. E.; Ogliaro, F.; Bearpark, M. J.; Heyd, J. J.; Brothers, E. N.; Kudin, K. N.; Staroverov, V. N.; Keith, T. A.; Kobayashi, R.; Normand, J.; Raghavachari, K.; Rendell, A. P.; Burant, J. C.; Iyengar, S. S.; Tomasi, J.; Cossi, M.; Millam, J. M.; Klene, M.; Adamo, C.; Cammi, R.; Ochterski, J. W.; Martin, R. L.; Morokuma, K.; Farkas, O.; Foresman, J. B.; Fox, D. J. *Gaussian 16*, Rev. C.01; Gaussian Inc., 2016.
- (61) Marenich, A. V.; Cramer, C. J.; Truhlar, D. G. Universal solvation model based on solute electron density and on a continuum model of the solvent defined by the bulk dielectric constant and atomic surface tensions. *J. Phys. Chem. B* **2009**, *113*, 6378–6396.
- (62) Becke, A. D. Density-functional thermochemistry. III. The role of exact exchange. *J. Chem. Phys.* **1993**, *98*, 5648–5652.
- (63) Lee, C.; Yang, W.; Parr, R. G. Development of the Colle-Salvetti correlation-energy formula into a functional of the electron density. *Phys. Rev. B* **1988**, *37*, 785–789.
- (64) Weigend, F.; Ahlrichs, R. Balanced basis sets of split valence, triple zeta valence and quadruple zeta valence quality for H to Rn: Design and assessment of accuracy. *Phys. Chem. Chem. Phys.* **2005**, *7*, 3297–3305.
- (65) Grimme, S.; Antony, J.; Ehrlich, S.; Krieg, H. A consistent and accurate ab initio parametrization of density functional dispersion correction (DFT-D) for the 94 elements H–Pu. *J. Chem. Phys.* **2010**, *132*, No. 154104.
- (66) Marcus, R. A.; Sutin, N. Electron transfers in chemistry and biology. *Biochim. Biophys. Acta, Bioenerg.* **1985**, *811*, 265–322.
- (67) Voityuk, A. A.; Rösch, N. Fragment charge difference method for estimating donor–acceptor electronic coupling: Application to DNA π -stacks. *J. Chem. Phys.* **2002**, *117*, 5607–5616.
- (68) Shao, Y.; Gan, Z.; Epifanovsky, E.; Gilbert, A. T.; Wormit, M.; Kussmann, J.; Lange, A. W.; Behn, A.; Deng, J.; Feng, X.; et al. Advances in molecular quantum chemistry contained in the Q-Chem 4 program package. *Mol. Phys.* **2015**, *113*, 184–215.
- (69) Marcus, R. A. Chemical and Electrochemical Electron-Transfer Theory. *Annu. Rev. Phys. Chem.* **1964**, *15*, 155–196.
- (70) Soudackov, A.; Hammes-Schiffer, S. Multistate continuum theory for multiple charge transfer reactions in solution. *J. Chem. Phys.* **1999**, *111*, 4672–4687.
- (71) Soudackov, A.; Hammes-Schiffer, S. Derivation of rate expressions for nonadiabatic proton-coupled electron transfer reactions in solution. *J. Chem. Phys.* **2000**, *113*, 2385–2396.
- (72) Hammes-Schiffer, S.; Soudackov, A. V. Proton-coupled electron transfer in solution, proteins, and electrochemistry. *J. Phys. Chem. B* **2008**, *112*, 14108–14123.
- (73) Poulos, T. L.; Kraut, J. The stereochemistry of peroxidase catalysis. *J. Biol. Chem.* **1980**, *255*, 8199–8205.
- (74) Derat, E.; Shaik, S. The Poulos–Kraut mechanism of compound I formation in horseradish peroxidase: A QM/MM Study. *J. Phys. Chem. B* **2006**, *110*, 10526–10533.
- (75) Derat, E.; Shaik, S.; Rovira, C.; Vidossich, P.; Alfonso-Prieto, M. The effect of a water molecule on the mechanism of formation of compound 0 in horseradish peroxidase. *J. Am. Chem. Soc.* **2007**, *129*, 6346–6347.
- (76) Vidossich, P.; Fiorin, G.; Alfonso-Prieto, M.; Derat, E.; Shaik, S.; Rovira, C. On the role of water in peroxidase catalysis: A theoretical investigation of HRP compound I formation. *J. Phys. Chem. B* **2010**, *114*, 5161–5169.
- (77) Zhang, X.; Jiang, Y.; Chen, Q.; Dong, S.; Feng, Y.; Cong, Z.; Shaik, S.; Wang, B. H-Bonding Networks Dictate the Molecular Mechanism of H₂O₂ Activation by P450. *ACS Catal.* **2021**, *11*, 8774–8785.
- (78) Jiang, Y.; Peng, W.; Li, Z.; You, C.; Zhao, Y.; Tang, D.; Wang, B.; Li, S. Unexpected Reactions of α , β -Unsaturated Fatty Acids Provide Insight into the Mechanisms of CYP152 Peroxygenases. *Angew. Chem., Int. Ed.* **2021**, *60*, 24694–24701.
- (79) Wang, B.; Zhang, X.; Fang, W.; Rovira, C.; Shaik, S. How Do Metalloproteins Tame the Fenton Reaction and Utilize •OH Radicals in Constructive Manners? *Acc. Chem. Res.* **2022**, *55*, 2280–2290.
- (80) Chreifi, G.; Baxter, E. L.; Doukov, T.; Cohen, A. E.; McPhillips, S. E.; Song, J.; Meharena, Y. T.; Soltis, S. M.; Poulos, T. L. Crystal structure of the pristine peroxidase ferryl center and its relevance to proton-coupled electron transfer. *Proc. Natl. Acad. Sci. U.S.A.* **2016**, *113*, 1226–1231.
- (81) Kwon, H.; Basran, J.; Casadei, C. M.; Fielding, A. J.; Schrader, T. E.; Ostermann, A.; Devos, J. M.; Aller, P.; Blakeley, M. P.; Moody, P. C.; Raven, E. L. Direct visualization of a Fe(IV)–OH intermediate in a heme enzyme. *Nat. Commun.* **2016**, *7*, No. 13445.
- (82) Lim, S. H.; Lee, W. S.; Kim, Y.-I.; Sohn, Y.; Cho, D. W.; Kim, C.; Kim, E.; Latham, J. A.; Dunaway-Mariano, D.; Mariano, P. S. Photochemical and enzymatic SET promoted C–C bond cleavage reactions of lignin β -1 model compounds containing varying number

of methoxy substituents on their arene rings. *Tetrahedron* **2015**, *71*, 4236–4247.

(83) Tuisel, H.; Sinclair, R.; Bumpus, J. A.; Ashbaugh, W.; Brock, B. J.; Aust, S. D. Lignin peroxidase H2 from *Phanerochaete chrysosporium*: purification, characterization and stability to temperature and pH. *Arch. Biochem. Biophys.* **1990**, *279*, 158–166.

(84) Romero, J. O.; Fernández-Fueyo, E.; Avila-Salas, F.; Recabarren, R.; Alzate-Morales, J.; Martínez, A. T. Binding and catalytic mechanisms of veratryl alcohol oxidation by lignin peroxidase: A theoretical and experimental study. *Comput. Struct. Biotechnol. J.* **2019**, *17*, 1066–1074.

(85) Gray, H. B.; Winkler, J. R. Long-range electron transfer. *Proc. Natl. Acad. Sci. U.S.A.* **2005**, *102*, 3534–3539.

(86) Balabin, I. A.; Hu, X.; Beratan, D. N. Exploring biological electron transfer pathway dynamics with the Pathways plugin for VMD. *J. Comput. Chem.* **2012**, *33*, 906–910.

(87) Wang, B.; Cao, Z. Mechanism of acid-catalyzed hydrolysis of formamide from cluster-continuum model calculations: concerted versus stepwise pathway. *J. Phys. Chem. A* **2010**, *114*, 12918–12927.

(88) Wang, B.; Johnston, E. M.; Li, P.; Shaik, S.; Davies, G. J.; Walton, P. H.; Rovira, C. QM/MM Studies into the H₂O₂-Dependent Activity of Lytic Polysaccharide Monooxygenases: Evidence for the Formation of a Caged Hydroxyl Radical Intermediate. *ACS Catal.* **2018**, *8*, 1346–1351.

(89) Peng, W.; Yan, S.; Zhang, X.; Liao, L.; Zhang, J.; Shaik, S.; Wang, B. How Do Preorganized Electric Fields Function in Catalytic Cycles? The Case of the Enzyme Tyrosine Hydroxylase. *J. Am. Chem. Soc.* **2022**, *144*, 20484–20494.

(90) Bím, D.; Alexandrova, A. N. Local Electric Fields as a Natural Switch of Heme-Iron Protein Reactivity. *ACS Catal.* **2021**, *11*, 6534–6546.

(91) Nilsen-Moe, A.; Rosichini, A.; Glover, S. D.; Hammarström, L. Concerted and Stepwise Proton-Coupled Electron Transfer for Tryptophan-Derivative Oxidation with Water as the Primary Proton Acceptor: Clarifying a Controversy. *J. Am. Chem. Soc.* **2022**, *144*, 7308–7319.

(92) Nilsen-Moe, A.; Reinhardt, C. R.; Glover, S. D.; Liang, L.; Hammes-Schiffer, S.; Hammarström, L.; Tommos, C. Proton-Coupled Electron Transfer from Tyrosine in the Interior of a de novo Protein: Mechanisms and Primary Proton Acceptor. *J. Am. Chem. Soc.* **2020**, *142*, 11550–11559.

(93) McEvoy, J. P.; Brudvig, G. W. Water-splitting chemistry of photosystem II. *Chem. Rev.* **2006**, *106*, 4455–4483.

(94) Cox, N.; Pantazis, D. A.; Lubitz, W. Current understanding of the mechanism of water oxidation in photosystem II and its relation to XFEL data. *Annu. Rev. Biochem.* **2020**, *89*, 795–820.

(95) Lomoth, R.; Magnuson, A.; Sjödin, M.; Huang, P.; Styring, S.; Hammarström, L. Mimicking the electron donor side of Photosystem II in artificial photosynthesis. *Photosynth. Res.* **2006**, *87*, 25–40.

(96) Sjödin, M.; Styring, S.; Åkermark, B.; Sun, L.; Hammarström, L. Proton-Coupled Electron Transfer from Tyrosine in a Tyrosine–Ruthenium–tris-Bipyridine Complex: Comparison with TyrosineZ Oxidation in Photosystem II. *J. Am. Chem. Soc.* **2000**, *122*, 3932–3936.

(97) Minnihan, E. C.; Nocera, D. G.; Stubbe, J. Reversible, long-range radical transfer in *E. coli* class Ia ribonucleotide reductase. *Acc. Chem. Res.* **2013**, *46*, 2524–2535.

(98) Reinhardt, C. R.; Li, P.; Kang, G.; Stubbe, J.; Drennan, C. L.; Hammes-Schiffer, S. Conformational Motions and Water Networks at the α/β Interface in *E. coli* Ribonucleotide Reductase. *J. Am. Chem. Soc.* **2020**, *142*, 13768–13778.

(99) Gray, H. B.; Winkler, J. R. Functional and protective hole hopping in metalloenzymes. *Chem. Sci.* **2021**, *12*, 13988–14003.

(100) Jones, S. M.; Transue, W. J.; Meier, K. K.; Kelemen, B.; Solomon, E. I. Kinetic analysis of amino acid radicals formed in H₂O₂-driven CuI LPMO reoxidation implicates dominant homolytic reactivity. *Proc. Natl. Acad. Sci. U.S.A.* **2020**, *117*, 11916–11922.

(101) Paradisi, A.; Johnston, E. M.; Tovborg, M.; Nicoll, C. R.; Ciano, L.; Dowe, A.; McMaster, J.; Hancock, Y.; Davies, G. J.;

Walton, P. H. Formation of a copper (II)–tyrosyl complex at the active site of lytic polysaccharide monooxygenases following oxidation by H₂O₂. *J. Am. Chem. Soc.* **2019**, *141*, 18585–18599.

(102) Sivaraja, M.; Goodin, D. B.; Smith, M.; Hoffman, B. M. Identification by ENDOR of Trp191 as the free-radical site in cytochrome c peroxidase compound ES. *Science* **1989**, *245*, 738–740.

(103) Yee, E. F.; Dzikovski, B.; Crane, B. R. Tuning radical relay residues by proton management rescues protein electron hopping. *J. Am. Chem. Soc.* **2019**, *141*, 17571–17587.

(104) Liu, T.; Tyburski, R.; Wang, S.; Fernández-Terán, R.; Ott, S.; Hammarström, L. Elucidating Proton-Coupled Electron Transfer Mechanisms of Metal Hydrides with Free Energy- and Pressure-Dependent Kinetics. *J. Am. Chem. Soc.* **2019**, *141*, 17245–17259.

(105) Dongare, P.; Maji, S.; Hammarström, L. Direct Evidence of a Tryptophan Analogue Radical Formed in a Concerted Electron–Proton Transfer Reaction in Water. *J. Am. Chem. Soc.* **2016**, *138*, 2194–2199.

(106) Irebo, T.; Zhang, M.-T.; Markle, T. F.; Scott, A. M.; Hammarström, L. Spanning Four Mechanistic Regions of Intramolecular Proton-Coupled Electron Transfer in a Ru(bpy)₃²⁺–Tyrosine Complex. *J. Am. Chem. Soc.* **2012**, *134*, 16247–16254.

(107) Tyson, K. J.; Davis, A. N.; Norris, J. L.; Bartolotti, L. J.; Hvastkovs, E. G.; Offenbacher, A. R. Impact of Local Electrostatics on the Redox Properties of Tryptophan Radicals in Azurin: Implications for Redox-Active Tryptophans in Proton-Coupled Electron Transfer. *J. Phys. Chem. Lett.* **2020**, *11*, 2408–2413.

(108) Pelletier, H.; Kraut, J. Crystal structure of a complex between electron transfer partners, cytochrome c peroxidase and cytochrome c. *Science* **1992**, *258*, 1748–1755.